Size and affinity kinetics of nanobodies influence targeting and penetration of solid tumours

Debie, P.; Lafont, C.; Defrise, M.; Hansen, I.; Willigen, D.M. van; Leeuwen, F.W.B. van; ... ; Hernot, S.

Journal of Controlled Release 317 (2020) 34–42

Contents lists available at ScienceDirect

Journal of Controlled Release

journal homepage: www.elsevier.com/locate/jconrel

Size and affinity kinetics of nanobodies influence targeting and penetration of solid tumours

Pieterjan Debie[a,*], Chrystel Lafont[b], Michel Defrise[a], Inge Hansen[a], Danny M. van Willigen[c], Fijs W.B. van Leeuwen[c], Rik Gijsbers[d], Matthias D'Huyvetter[a], Nick Devoogdt[a], Tony Lahoutte[a,e], Patrice Mollard[b], Sophie Hernot[a]

[a] Laboratory for In vivo Cellular and Molecular Imaging, ICMI-BEFY, Vrije Universiteit Brussel, Brussels, Belgium
[b] Institut de Génomique Fonctionnelle, CNRS, INSERM, Univ. Montpellier, Montpellier, France
[c] Interventional Molecular Imaging laboratory, Department of Radiology, Leiden University Medical Center, Leiden, the Netherlands
[d] Laboratory for Molecular Virology and Gene therapy, Department of Pharmaceutical and Pharmacological Sciences, KU Leuven, Leuven, Belgium
[e] Department of Nuclear Medicine, UZBrussel, Brussels, Belgium

ARTICLE INFO

Keywords:
Single-domain antibodies
Intravital imaging
Tumour distribution
Targeted therapy
Molecular imaging

ABSTRACT

A compound's intratumoural distribution is an important determinant for the effectiveness of molecular therapy or imaging. Antibodies (Abs), though often used in the design of targeted compounds, struggle to achieve a homogenous distribution due to their large size and bivalent binding mechanism. In contrast, smaller compounds like nanobodies (Nbs) are expected to distribute more homogenously, though this has yet to be demonstrated *in vivo* at the microscopic level. We propose an intravital approach to evaluate the intratumoural distribution of different fluorescently labeled monomeric and dimeric Nb tracers and compare this with a monoclonal antibody (mAb).

Monomeric and dimeric formats of the anti-HER2 (2Rb17c and 2Rb17c-2Rb17c) and control (R3B23 and R3B23-R3B23) Nb, as well as the dimeric monovalent Nb 2Rb17c-R3B23 were generated and fluorescently labeled with a Cy5 fluorophore. The mAb trastuzumab-Cy5 was also prepared. Whole-body biodistribution of all constructs was investigated in mice bearing subcutaneous xenografts (HER2+ SKOV3) using *in vivo* epi-fluorescence imaging. Next, for intravital experiments, GFP-expressing SKOV3 cells were grown under dorsal window chambers on athymic nude mice (n = 3/group), and imaged under a fluorescence stereo microscope immediately after intravenous injection of the tracers. Consecutive fluorescence images within the tumour were acquired over the initial 20 min after injection and later, single images were taken at 1, 3 and 24 h post-injection. Additionally, two-photon microscopy was used to investigate the colocalization of GFP (tumour cells) and Cy5 fluorescence (tracers) at higher resolution.

Whole-body images showed rapid renal clearance of all Nbs, and fast tumour targeting for the specific Nbs. Specific tumour uptake of the mAb could only be clearly distinguished from background after several hours. Intravital imaging revealed that monomeric Nb tracers accumulated rapidly and distributed homogenously in the tumour mere minutes after intravenous injection. The dimeric compounds initially achieved lower fluorescence intensities than the monomeric. Furthermore, whereas the HER2-specific dimeric bivalent compound remained closely associated to the blood vessels over 24 h, the HER2-specific dimeric monovalent tracer achieved a more homogenous tumour distribution from 1 h post-injection onwards. Non-specific tracers were not retained in the tumour. Trastuzumab had the most heterogenous intratumoural distribution of all evaluated compounds, while -due to the long blood retention- achieving the highest overall tumour uptake at 24 h post-injection.

In conclusion, monomeric Nbs very quickly and homogenously distribute through tumour tissue, at a rate significantly greater than dimeric Nbs and mAbs. This underlines the potential of monomeric Nb tracers and therapeutics in molecular imaging and targeted therapies.

* Corresponding author.
E-mail address: pieterjan.debie@vub.be (P. Debie).

https://doi.org/10.1016/j.jconrel.2019.11.014
Received 6 September 2019; Received in revised form 10 November 2019; Accepted 12 November 2019
Available online 14 November 2019

1. Introduction

In oncology, targeted therapies and molecular imaging techniques are increasingly entering clinical practice. They make use of compounds that specifically interact with molecular targets involved in the pathophysiology of cancer. These compounds can be used directly as therapeutic agents, by inhibiting ligand binding to receptors and/or by activating immune effector functions [1]. Alternatively, they can be conjugated to a toxic agent such as a cytotoxic chemical or high-energy radio-isotope. In analogy, for imaging applications, a reporter molecule *e.g.* a diagnostic radioisotope or fluorescent dye, is conjugated to the targeting moiety [2].

For optimal performance, it is important that such targeted agents penetrate the tumour efficiently. Solid tumours have particular properties that influence this process [3,4]. While the heightened fenestration of tumour vasculature and diminished or absent lymphatic drainage mechanisms allow the accumulation of large compounds due to the so-called enhanced permeability and retention (EPR) effect [5], the microvasculature's heterogenous permeability as well as increased interstitial pressure counteract this [4,6]. The limited or absent pressure gradient into the tumour means that transport occurs mainly through diffusion instead of convection. And importantly, the rate of diffusion is known to be inversely related to the size of the diffusing molecule [7].

Traditionally, antibodies (Abs) have been widely applied as targeting agents by exploiting their high specificity and affinity. Furthermore, the versatility of their paratope allows Abs to be conveniently generated against virtually any antigen of interest. However, their large size (~150 kDa) prevents efficient diffusion through tumour tissue and it has been shown that Ab-based compounds are subject to the 'binding-site-barrier' effect, where due to their high avidity, they remain close to the periphery of the vasculature [8–10]. Additionally, because of their large size and neonatal Fc receptor (FcRn)-mediated recycling, Abs have long blood half-lives of several days to weeks [11]. This property allows Ab-tracers to achieve high uptake-values in targeted tissues, but simultaneously leads to elevated overall non-specific accumulation. To achieve faster pharmacokinetics and a more homogenous tumour distribution, the use of smaller and monomeric targeting agents is often considered. Their reduced size should allow for more easy extravasation into, and diffusion through the tumour tissue, while being rapidly cleared from the blood [12–16].

Nanobodies (Nbs) are the antigen-binding domains of heavy-chain only Abs found in members of the Camelid family, and are the smallest stable Ab fragments available [17,18]. In the last decade, they have been broadly explored as novel targeting moieties for molecular imaging and therapy [19]. Indeed, when conjugated with radio-isotopes or fluorescent dyes, their rapid targeting and fast blood clearance allows for high tumour-specific uptake, with low background. This results in high contrast images early after injection in the case of molecular imaging, and the application of higher doses of therapeutic radionuclides with limited toxicity [20–27].

It has often been stated than Nbs can rapidly achieve a homogenous intratumoural distribution. While some studies have investigated this aspect *via ex vivo* analysis on tumour slices or using *in vitro* spheroids [28–32], this has not yet been clearly demonstrated at a microscopic level *in vivo*. Therefore, the objective of this study was to evaluate the intratumoural distribution of a tumour-specific Nb, and to investigate the impact of increased size and valency on tumour penetration. This was achieved using an intravital fluorescence microscopy approach, in combination with whole body macroscopic epi-fluorescence imaging.

2. Materials & methods

2.1. Preparation and fluorescent labeling of the Ab and Nb-tracers

The tumour-specific Nb 2Rb17c, recognizing the epidermal growth factor receptor 2 (HER2), and the non-targeting control Nb R3B23, specific for the 5 T2 mouse myeloma idiotype, were generated in previous studies [33,34]. In addition, these Nbs were used to create dimeric constructs, namely, the dimeric bivalent Nb 2Rb17c-2Rb17c, the dimeric monovalent Nb 2Rb17c-R3B23 and the dimeric control Nb R3B23-R3B23 according to previously described methods [21,30]. In brief, dimeric Nbs were constructed by inserting a DNA sequence encoding for the linker amino acid sequence '$(GGGGS)_3$' connecting the C-terminal end of one Nb with the N-terminal end of the other. All Nb-formats, expressing a C-terminal hexahistidine-tag, were expressed in *E. coli* and subsequently purified using immobilized metal affinity chromatography (IMAC) and size exclusion chromatography (SEC). Trastuzumab was obtained from Roche. The steady-state affinity of the HER2-specific compounds, as well as the association and dissociation kinetics were determined using surface plasmon resonance (Biacore T200, GE Healthcare), on HER2-Fc protein immobilized using a CM5-chip (GE Healthcare) as described before [33]. Binding parameters were determined using BIAevaluation software (GE Healthcare) and represented using either the same software or Prism 7 (GraphPad).

The well characterized Cy5-$N^+(Me)_3$ fluorophore was synthesized as previously described [35,36] and the preparation of OSu-Cy5-$N^+(Me)_3$ (Mw. 825) was performed according to Spa et al. [37]. The last reaction was monitored using a Waters (Etten-Leur, The Netherlands) HPLC system equipped with a 1525EF pump, a 2489 UV/Vis detector and a Dr. Maisch GmbH (Ammerbuch, Germany) Reprosil-Pur C18-AQ 5 μm (250 × 4.6 mm) column applying a gradient of 0.1% TFA in H_2O/Acetonitrile 95:5 to 0.1% TFA in H_2O/Acetonitrile 5:95 in 40 min (1 mL/min). After 2 h, the OSu-Cy5-$N^+(Me)_3$ product was precipitated in ethyl acetate, washed twice with ethyl acetate and dried in a desiccator. HPLC purity was > 95%. Hereafter OSu-Cy5-$N^+(Me)_3$ was randomly conjugated to the different Nb-formats according to standard amino-acid conjugation chemistry. A 5-fold molar excess of the fluorophore (dissolved at 20 mg/mL in DMSO) was incubated for 2 h with the Nb/Ab (1 mg/mL) at pH 8.3–8.5. Cy5-labeled compounds were then purified by SEC on a Superdex 75 10/300 GL column (GE Healthcare) with PBS (pH 7.4) as elution buffer (0.5 mL/min). Quality control of the purified tracers was performed by analytical SEC using a Superdex 75 15/150 GL column with PBS (pH 7.4) as elution buffer (0.3 mL/min). Purity of the compounds was further investigated by SDS-PAGE in reducing conditions using a Novex 8–16% Tris-Glycine gel (Thermo Fisher Scientific). The fluorophore to Nb/Ab ratio was determined by absorbance measurement at wavelengths of 280 (Nb/Ab) and 650 nm (Cy5 fluorophore) using a Nanodrop2000 spectrophotometer (Thermo Fisher Scientific). To account for the contribution of the fluorophore, the measured absorbance at 280 nm was corrected by subtracting 5% of the absorbance at 650 nm.

2.2. Whole body biodistribution of the tracers

The *in vivo* biodistribution study was approved by the Ethical Committee for Animal Experiments of the Vrije Universiteit Brussel (15-272-5). In order to prevent autofluorescence interference from chlorophyll in the gastrointestinal tract, the mice were fed a lowly fluorescent chow (Teklad 2016, Envigo). On the right hind limb of athymic nude Crl:NUFoxn1^{NU} mice (Charles River) (n = 3 per group), $5*10^6$ SKOV3 (HER2-expressing) cells were inoculated subcutaneously. Tumours were allowed to grow until they reached a size between 100 and 250 mm^3. 2 nmol of the tracer (based on fluorophore concentration) was injected intravenously *via* the tail vein. At 1 and 24 h post-injection epi-fluorescence images of the ventral and dorsal side of the animals were taken using the FMT2500 (PerkinElmer) operating in the 635 nm channel. White light images were overlaid with fluorescence images for anatomical localization. Images were analyzed using TrueQuant software (Perkin Elmer).

2.3. Dorsal window tumour model

The study protocol related to the intravital imaging experiment was approved by the Languedoc Roussillon Institutional Animal Care and Use Committee (APAFIS#4997-20 16041418239399 v5). For preparation of the dorsal window tumour model, Swiss Foxn1 Nude mice (Janvier Labs) were anesthetized by intraperitoneal Ketamine (100 mg/kg)/Xylazine (10 mg/kg) injection. Along the midline of the mouse's back, the two halves of the dorsal window chamber were aligned and sutured together. When the chamber was properly positioned, one layer of skin was removed completely. $5*10^6$ green fluorescent protein (GFP) transfected SKOV3 cells, were subsequently implanted under the fascia of the remaining layer of skin. These cells were generated using a lentiviral vector which was produced as previously described [38]. Finally, the chamber was assembled using close fitting transparent windows. Tumours were imaged thrice weekly in the GFP channel of a Discovery V12 microscope (Zeiss) to monitor tumour development, until full vascularization occurred (10 days post-implantation).

2.4. Fluorescence stereo microscope imaging

Mice ($n = 3$ per group) were anesthetized by isoflurane inhalation (5% for induction, 2.5% for maintenance) and placed with the dorsal window chamber positioned directly under the Discovery V12 microscope. The position was adjusted based on the location of the tumour, which could be located by visualizing the GFP signal. 2 nmol of tracer (based on the concentration of the fluorophore) was intravenously injected *via* the tail vein. From the moment of injection, sequential images were acquired at 100× magnification (1346 μm × 1346 μm) in the Cy5 channel for 10 min at a frequency of 2 Hz, and for an additional 10 min with a frequency of 0.5 Hz. Afterwards, additional single Cy5 images of the same site were taken at 1, 3 and 24 h post-injection using identical conditions.

2.5. Two-photon microscopy imaging

At 1 h, 3 h and 24 h, immediately after stereo microscopic imaging, the mice ($n = 3$ per group) were again anesthetized by isoflurane inhalation (5% for induction, 2.5% for maintenance) and placed with the dorsal window chamber positioned directly under a Zeiss 7MP two-photon microscope (20×, 1 NA, 2 mm WD). Multiphoton excitation was achieved using a mode-locked Ti:Sapphire Laser Chameleon (Coherent Inc.) tuned at 820 nm (for both eGFP and Cy5 excitation). Emitted fluorescence was captured using GaAsP photomultiplier tubes at 500–550 nm and > 590 nm for GFP and Cy5, respectively. A zone within the tumour was chosen where both GFP and Cy5 signals occurred (no Cy5 signal could be detected for control compounds). Then, 8-bit (0–255 grey levels; 379.5 μm × 272.8 μm) images were acquired with the Zeiss software Zen 2.1 (black) and analyzed with ImageJ.

2.6. Analysis of the intravital images obtained using the fluorescence stereo microscope

Sequential 16-bit images obtained during the intravital imaging experiment using the stereo microscope, were first aligned using the template matching plugin of ImageJ to correct for small movements of the dorsal window chamber over time. Next, a circular region of interest (ROI) of the same size and at the same position within individual animals, was defined in each image based on the GFP fluorescence. On the initial reference frame, acquired just before injection of the tracer, the fluorescence background signal was determined as the lowest intensity value in the ROI. The overall fluorescence intensity increase in the tumour over time was calculated by measuring the total intensity in the ROI at the different timepoints using ImageJ and subtracting the background. These values were graphically represented using Prism 7 software (GraphPad).

In addition, the extent of extravasation and homogenous tumour penetration of the different tracers was quantified using Amide software over the first 10 min post-injection with a simple empirical method, inspired by 2D isotropic diffusion from the blood vessels. For each animal, the initial reference frame when the tracer had just filled the blood vessels was identified. The analysis was performed in the same ROI used for the quantification of the fluorescence intensity, to avoid impact of the image borders. Each subsequent frame is modelled as a blurred version of the reference frame, with a blurring described by a 2D Gaussian function. The width (FWHM) of the 2D Gaussian function that optimizes the fit between the frame and the blurred reference frame is recorded and used to empirically characterize the time course of the tracer penetration.

The procedure is summarized in Eqs. (1)–(4), where (x,y) are the image coordinates and the integrals are discretized as usual as sums over the pixels. The 2D Gaussian kernel with standard deviation σ in Eq. (1) is convolved with the selected reference frame $f_{ref}(x,y)$ (Eq. (2)) to obtain the blurred reference frame $f^{\sigma}_{ref}(x,y)$. For each frame (with index t) the relative squared error (3) with the blurred reference frame is minimized by varying σ, and the minimum value is converted to the FWHM (Eq. (4)). Evaluation of the intratumoural distribution of all compounds at timepoints later than 10 min post-injection was not possible using the gaussian distribution model, because images obtained after replacing the animals under the intravital microscope could not be perfectly aligned.

$$k_\sigma(x,y) = \frac{1}{2\pi\sigma^2}\exp\left(-\frac{x^2+y^2}{2\sigma^2}\right) \tag{1}$$

$$f^{\sigma}_{ref}(x,y) = \iint dx'dy' f_{ref}(x',y')k_\sigma(x-x',y-y') \tag{2}$$

$$e^{\sigma}_t(\sigma) = \frac{\iint_{ROI} dx\ dy\ |f^{\sigma}_{ref}(x,y) - f_t(x,y)|^2}{\iint_{ROI} dx\ dy\ |f^{\sigma}_{ref}(x,y)|^2} \tag{3}$$

$$FWHM^{min}_t = 2\sqrt{2\ln(2)}\sigma^{min}_t \tag{4}$$

3. Results

3.1. Preparation of the fluorescent tracers

The monomeric and dimeric anti-HER2 and control Nb constructs, as well as the mAb trastuzumab, were successfully conjugated with the Cy5 fluorophore. Analytical chromatography demonstrated that the purity for all products was above 95% (Fig. S1). Dye-to-protein ratios for all compounds ranged between 0.8 and 0.9 (Table S1).

The affinities of the HER2-specific Nbs, along with trastuzumab were determined by surface plasmon resonance (Fig. 1, Tables 1A and 1B, Fig. S3). To discount the influence of bivalent binding on the measured affinity, steady-state affinities were compared. As can be seen in Table 1A, all HER2-specifc compounds exhibited similar affinities in the low nanomolar range. The effect of increased valency could be perceived in the dissociation kinetics, with the bivalent tumour-specific Nb 2Rb17c-2Rb17c and trastuzumab dissociating much more slowly (Fig. 1A, Table 1B).

3.2. In vivo whole-body biodistribution

The general biodistribution and tumour targeting potential of the tracers was evaluated by non-invasive epi-fluorescence imaging (Fig. 2). All Nb-tracers were rapidly cleared from the circulation *via* the kidneys, resulting in low background fluorescence. Both monomeric and dimeric anti-HER2 Nbs exhibited specific tumour uptake 1 h post-injection and the signal, although diminished, remained visible until at least 24 h. No tumour uptake was seen for the control monomeric or dimeric Nb tracers. As expected for Abs, higher overall background

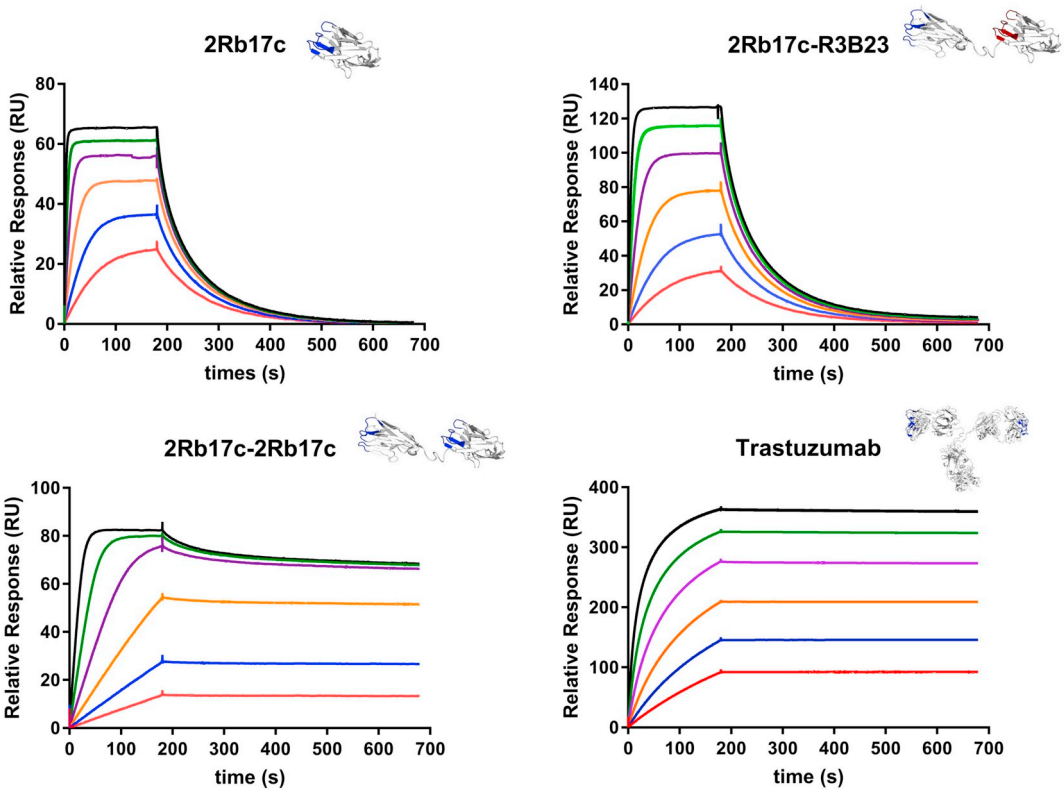

Fig. 1. SPR data of HER2-binding compounds on recombinant HER2 protein. A: Association and dissociation kinetics of anti-HER2 monovalent and bivalent Nb-constructs as well as trastuzumab. Dilution series: 2Rb17c and 2Rb17c-R3B23 from 125.0 nM to 3.9 nM; 2Rb17c-2Rb17c from 15.6 to 0.5 nM; trastuzumab from 62.5 to 2.0 nM.

Table 1A
Steady-state affinities (K_D) of anti-HER2 compounds as determined by SPR.

Steady-state affinity	K_D (nM)
Compound	
2Rb17c	5.51 ± 0.51
2Rb17c-R3b23	9.14 ± 0.27
2Rb17c-2Rb17c	3.47 ± 1.90
Trastuzumab	7.97 ± 0.27

fluorescence was observed for trastuzumab, with tumour uptake increasing greatly over 24 h.

3.3. Intravital imaging with fluorescence stereo microscopy

To investigate *in vivo* and longitudinally the distribution of the different tracers in tumour tissue at microscopic level, intravital imaging of well-vascularized tumours grown under a dorsal window chamber was performed (see Fig. S4 for experimental setup). Videos acquired over the first 10 min following injection of the tracers can be found in the supplementary data.

An overview of representative images taken at different time points over 24 h at the same location in the tumour is given in Fig. 3. These demonstrate that both the HER2-specific as well as control monomeric Nbs extravasated and penetrated rapidly into the tumour tissue, achieving a seemingly homogenous intratumoural distribution within the first minutes after injection. The rapid homogenous distribution of 2Rb17c was also confirmed in the Gaussian distribution graph (Fig. 4), where the pre-determined maximal homogeneity, shown as the blurring of the initial reference image, is already achieved 2 min post-injection. Additionally, as shown in Fig. 5, mean fluorescence intensities measured over 24 h demonstrate that the maximal value was already reached between 2 and 5 min post-injection. Whereas 2Rb17c retained 89.5 ± 5.6% of its maximal fluorescence intensity after 1 h and

Table 1B
Binding kinetics (association (k_a) and dissociation (k_d) rates) of anti-HER2 compounds as determined by SPR, taking the monovalent or bivalent binding mechanism into account.

Binding kinetics				
Monovalent compounds		k_a (1/M.s)		k_d (1/s)
2Rb17c		$(7.07 \pm 0.01)*10^{6}$		$(3.03 \pm 0.01)*10^{-2}$
2Rb17c-R3b23		$(3.29 \pm 0.01)*10^{6}$		$(2.68 \pm 0.01)*10^{-2}$
Bivalent compounds	k_{a1} (1/M.s)	k_{a2} (1/RU.s)	k_{d1} (1/s)	k_{d2} (1/s)
2Rb17c-2Rb17c	$(3.80 \pm 0.01)*10^{6}$	$(9.57 \pm 0.03)*10^{-3}$	$(1.80 \pm 0.01)*10^{-2}$	$(1.58 \pm 0.01)*10^{-3}$
Trastuzumab	$(4.70 \pm 0.01)*10^{5}$	$(4.14 \pm 0.10)*10^{-3}$	$(2.50 \pm 0.07)*10^{-5}$	$(1.61 \pm 0.35)*10^{-1}$

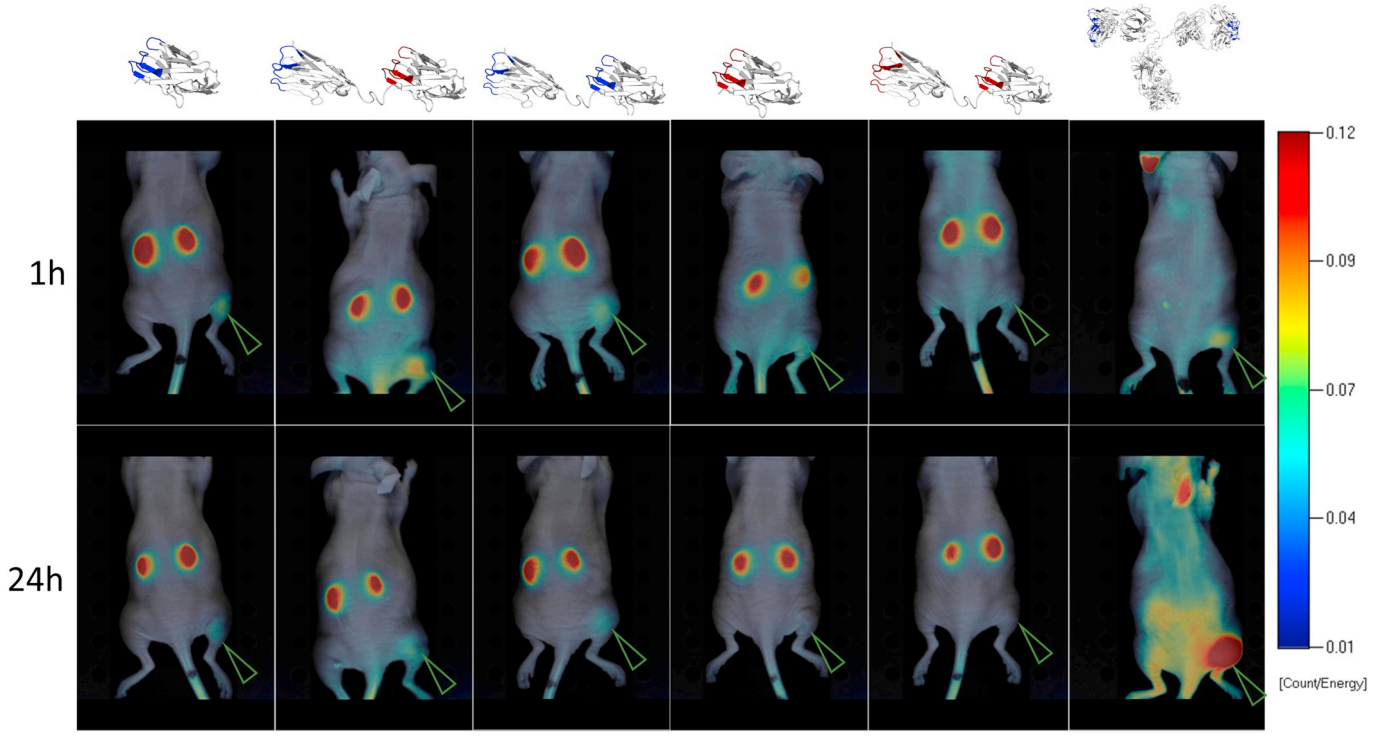

Fig. 2. Whole-body biodistribution profiles at 1 and 24 h post-injection of different fluorescently-labeled Nb-based constructs and an Ab in mice with a HER2-positive subcutaneous xenograft. Tumours are indicated by the green arrow. From left to right: 2Rb17c, 2Rb17c-R3B23, 2Rb17c-2Rb17c, R3B23, R3B23-R3B23, and trastuzumab. (For interpretation of the references to colour in this figure legend, the reader is referred to the web version of this article.)

61.3 ± 3,5% after 24 h, the maximal intensity of R3B23 was already reduced by 59.4 ± 12.2% after 20 min and was, with 0.7 ± 1.0% of the maximal intensity remaining, practically fully cleared after 24 h.

The dimeric Nbs extravasated and accumulated into the tumour more slowly than the monomeric variants. This resulted in a reduced overall accumulation in the tumour tissue for the bivalent Nb 2Rb17c-2Rb17c compared to 2Rb17c, though it was retained longer. Indeed, the signal intensity of 2Rb17c-2Rb17c remained very similar from 1 h

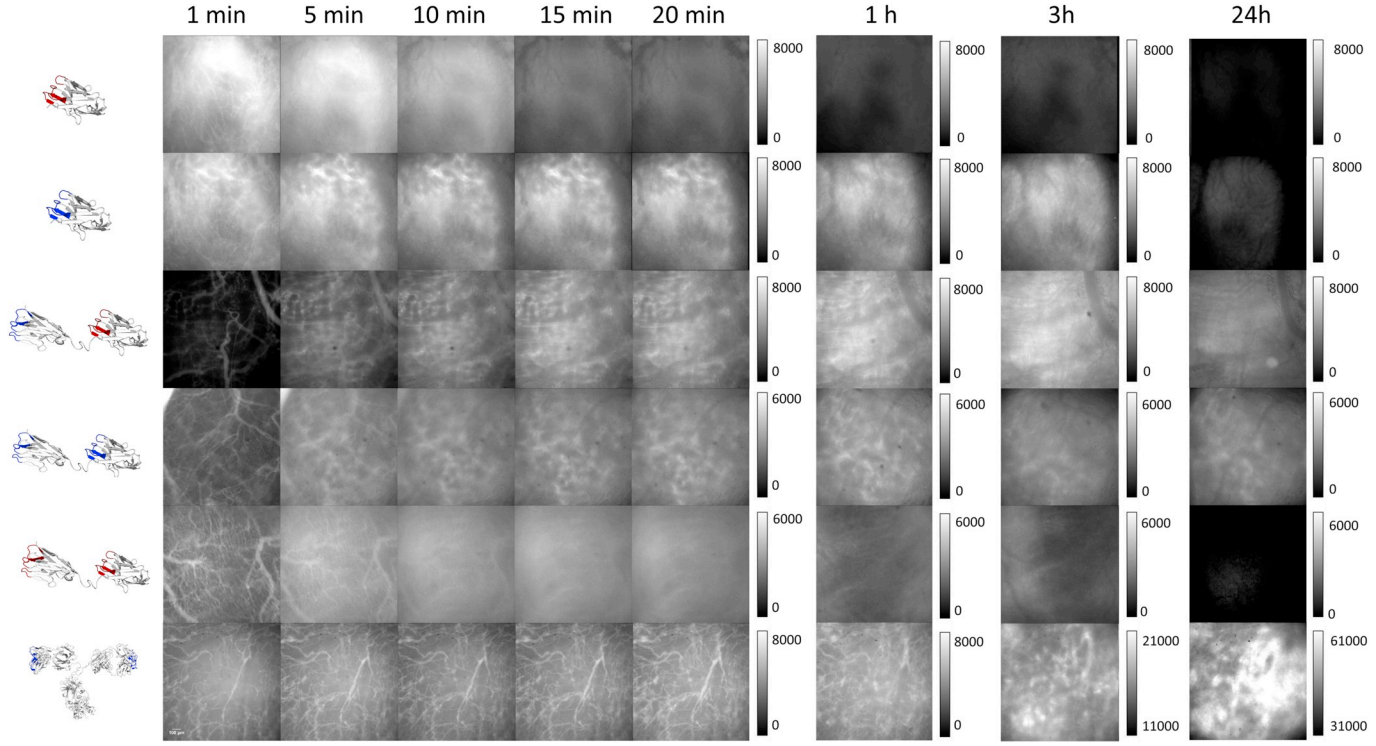

Fig. 3. Representative intravital images acquired in tumour tissue, using fluorescence stereo microscopy, over 24 h after injection of various fluorescently-labeled Nb-based constructs and a monoclonal antibody. Images are background subtracted, and the background was determined as the intensity in the imaging window before injection of the tracers. Scalebars are expressed in counts. From top to bottom: R3B23, 2Rb17c, 2Rb17c-R3B23, 2Rb17c-2Rb17c, R3B23-R3B23, and trastuzumab.

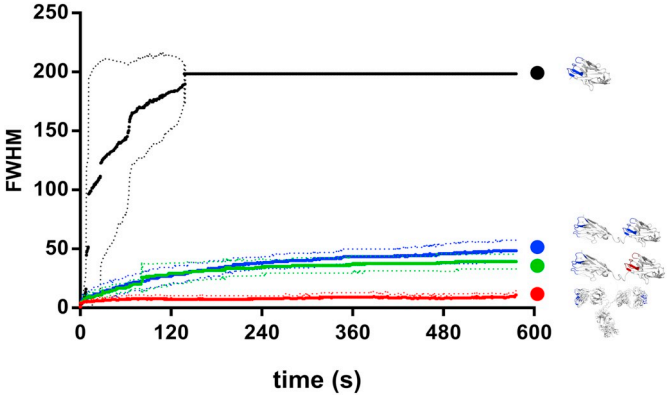

Fig. 4. Gaussian distribution of HER2-specific Nb-based constructs and a HER2-specific Ab from blood vessels. Images at different timepoints were matched with different degrees of gaussian blurring from the initial reference image. Higher values correspond to a greater degree of distribution, and correspondingly greater intratumoural homogeneity. Top to bottom: 2Rb17c, 2Rb17c-2Rb17c, 2Rb17c-R3B23, and trastuzumab.

onwards, increasing only by 14.2 ± 22.9% to the maximal value reached after 24 h, this signal was furthermore overall much higher than for R3B23-R3B23 (Fig. 5). The bivalent Nb 2Rb17c-2Rb17c furthermore did not achieve a homogenous intratumoural distribution, even after 24 h, as the region of highest fluorescence intensity mainly remained localized in close proximity to the blood vessels (Figs. 3 and 4). Contrarily, while initially the dimeric monovalent Nb 2Rb17c-R3B23 showed uptake levels and a heterogenous intratumoural distribution similar to the bivalent specific Nb, from 1 h post-injection onwards a more homogenous profile was seen (Figs. 3 and 4). Furthermore, for this Nb-tracer the maximal mean fluorescence intensity was achieved between 1 h and 3 h post-injection, with values higher than for the bivalent dimeric Nbs. After 24 h, 65.6 ± 27.6% of the maximal mean fluorescence intensity persisted (Fig. 5).

As shown in Figs. 3 and 4, in the first 3 h after injection, the mAb trastuzumab remained clearly visible within the vasculature, with no to very limited extravasation. After that, signal intensity in the tumour increased greatly (over 11-fold increase at 24 h compared to maximal intensity value at 1 h). The maximal fluorescence intensity achieved with trastuzumab was furthermore at least 7-fold higher than the maximal fluorescence intensity obtained with monomeric and dimeric monovalent Nbs, and over 10-fold higher than the maximal intensity of the dimeric bivalent Nb (Fig. 5). Nevertheless, it was also apparent that over time the intratumoural spread remains highly heterogenous, with fluorescence signals located perivascularly (Fig. 3).

3.4. Intravital imaging with two-photon microscopy

In addition to the stereo microscopic images, two-photon microscopy was used to acquire higher resolution images within a more limited field of view in the tumour area. Representative images taken at 1, 3 and 24 h post-injection of the different tracers are displayed in Fig. 6. As evidenced by the colocalization of GFP and Cy5 fluorescence signals, the HER2-specific compounds specifically associated with SKOV3 cells. While signal-intensity for 2Rb17c and 2Rb17c-R3b23 decreased by 24 h compared to the earlier time points, the dimeric bivalent Nb 2Rb17c-2Rb17c on the other hand was clearly retained in the tumour. No specific Cy5 fluorescence could be observed for the non-specific Nbs. Finally, the mAb trastuzumab showed only limited targeting of the tumour cells at 1 h post-injection, nevertheless, signal-intensity notably increased over time, especially by 24 h post-injection.

4. Discussion

It is widely recognized that smaller molecules such as Ab-fragments and low-molecular weight protein scaffolds can penetrate solid tumour tissue more efficiently than intact Abs [39]. As Nbs are an interesting class of Ab-fragments that is increasingly being investigated for molecular therapy and imaging applications, we aimed to evaluate their intratumoural distribution *in vivo*, and investigate in a longitudinal way the impact of size and (bi)valency on their capacity to penetrate tumour tissue. Hereto, different fluorescently-labeled anti-HER2 monomeric and dimeric Nb-constructs, along with their non-specific counterparts and a HER2-specific mAb, were evaluated both in a subcutaneous xenograft model for macroscopic non-invasive fluorescence imaging as

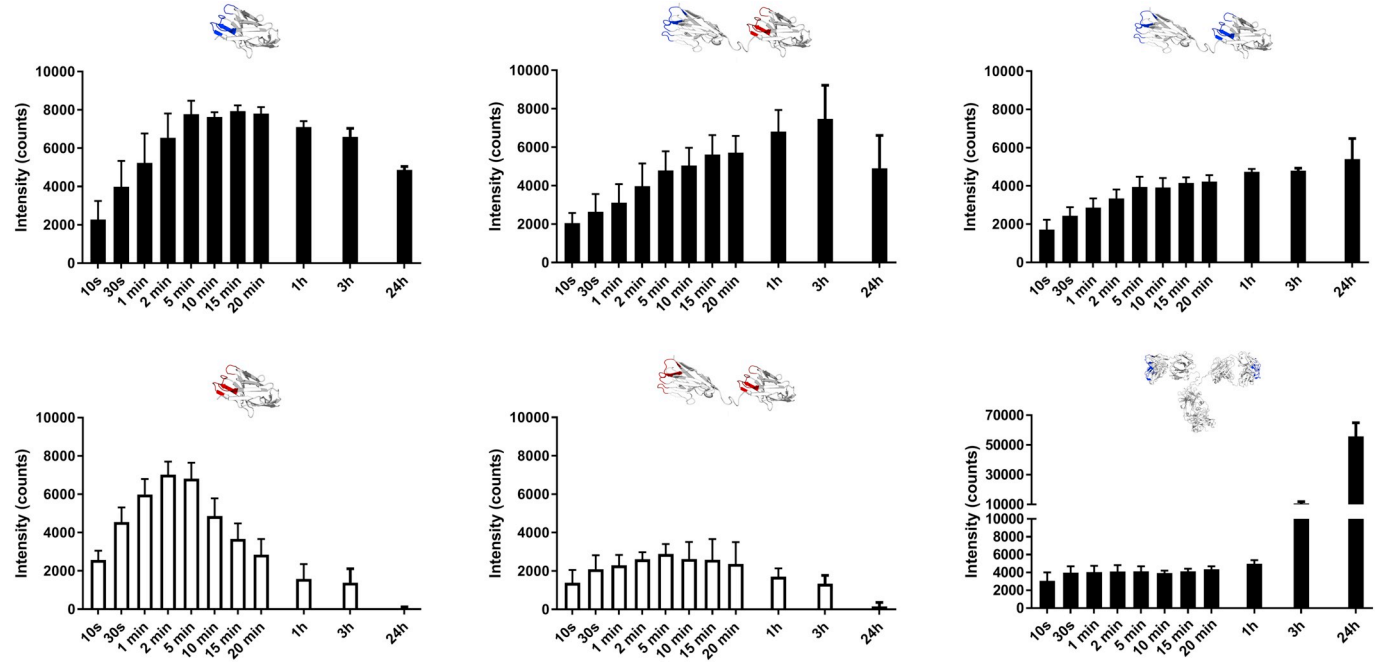

Fig. 5. Mean fluorescence intensities measured in the tumour imaging window at different timepoints over 24 h after intravenous injection of different fluorescently-labeled Nb-constructs and an Ab. Top left to right: 2Rb17c, 2Rb17c-R3B23, and 2Rb17c-2Rb17c. Bottom left to right: R3B23, R3B23-R3B23, and trastuzumab.

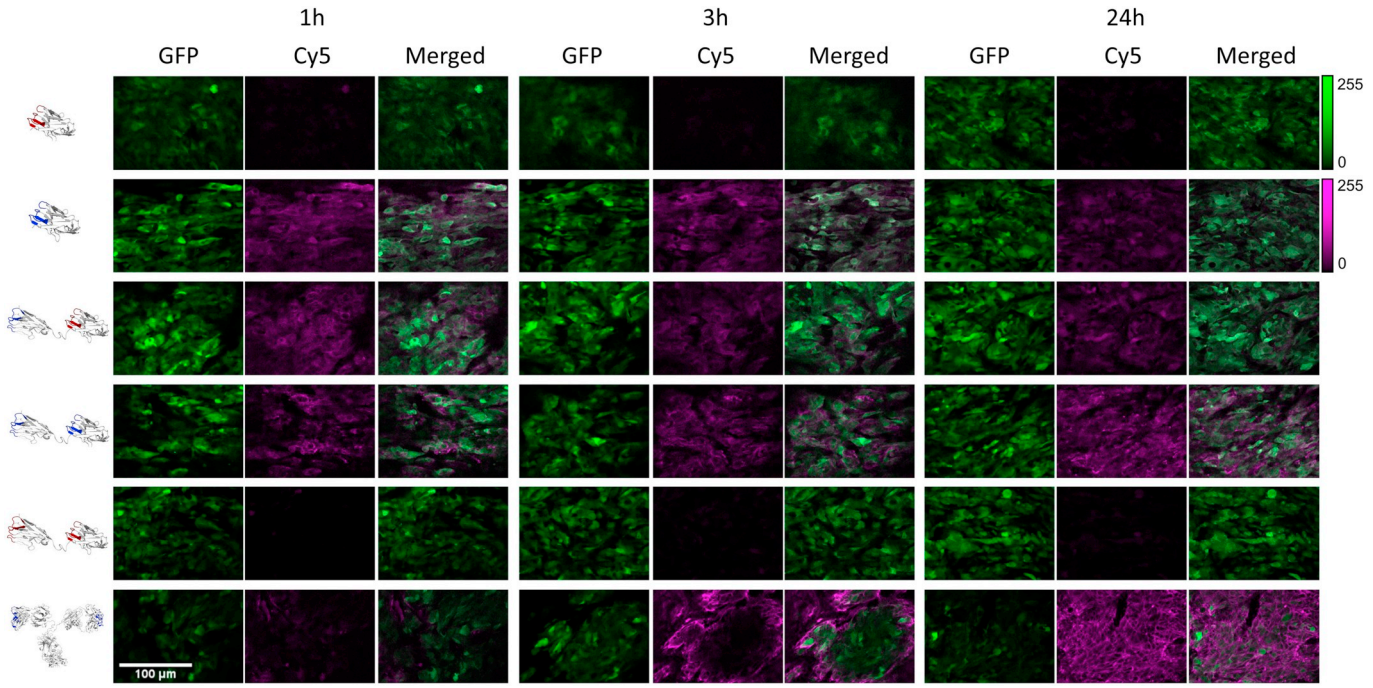

Fig. 6. Representative two-photon microscopic images taken in the tumour area at 1, 3 and 24 h post-injection of all constructs. Green signal corresponds to GFP expression by the tumour cells, whereas the purple signal denotes Cy5 fluorescence. Areas were chosen based on the presence of both GFP and Cy5 signal, where applicable. Scalebars are expressed in grey levels. From top to bottom: R3B23, 2Rb17c, 2Rb17c-R3B23, 2Rb17c-2Rb17c, R3B23-R3B23, and trastuzumab. (For interpretation of the references to colour in this figure legend, the reader is referred to the web version of this article.)

well as in a dorsal window chamber model allowing real-time microscopic imaging inside the tumour tissue itself.

All HER2-specific Nb-based tracers exhibited the general biodistribution profile expected for intravenously injected, hydrophilic protein tracers with a molecular weight smaller than 60 kDa, *i.e.* rapid blood clearance, renal excretion, and fast and specific tumour uptake [11]. Although quantitative assessment of *in vivo* epi-fluorescence images is not very accurate, no major visual differences could be remarked between monomeric (~15 kDa) and dimeric Nb constructs (~30 kDa). The binding of the different HER2-specific tracers to the SKOV3 tumour cells, as well as the absence of targeting for the control compounds, was furthermore confirmed by two-photon microscopy.

When tumour penetration was investigated at microscopic level using fluorescence stereo microscopy, it was confirmed that specific monomeric Nbs achieve maximal uptake and homogenous intratumoural distribution mere minutes after intravenous injection and that non-specific accumulation in tumour tissue is already largely eliminated after 20 min. Contrarily, dimeric Nbs accumulate slightly slower and reach a lower fluorescence intensity than the monomeric ones, most likely due to their larger size that hinders extravasation and decelerates diffusion. The increased avidity of bivalent Nbs as compared to their monovalent monomeric or dimeric counterparts, results on the one hand in a steady tumour retention over at least 24 h, and on the other hand in a restricted localization of the Nb close to the perivascular space. The latter effect, known as the binding-site barrier effect, was also clearly observed with the mAb trastuzumab. Moreover, because of trastuzumab's long blood half-life, maximal tumour uptake was only achieved at the 24 h time-point and was significantly higher than for the Nb-constructs. This is in accordance with the non-invasive macroscopic fluorescence imaging results obtained in this study, and corroborates previous observations regarding the pharmacokinetics of radio- and fluorescently-labeled Nb-based tracers. For instance, Krasniqi et al. recently demonstrated that a bivalent anti-CD20 Nb with a tumour uptake of 4.22 ± 0.90% injected activity per gram (%IA/g) after 1 h, was with 2.63 ± 0.31%IA/g remaining after 24 h retained significantly longer in CD20-expressing xenografts than the same, but monomeric Nb. For the latter, only 0.55 ± 0.09% IA/g remained after 24 h from 4.82 ± 1.80% IA/g after 1 h. Similarly, drastically reduced tumour uptake was seen with a bivalent Nb-construct recognizing the macrophage mannose receptor (MMR) expressed on alternatively activated tumour-associated macrophages [31].

Other groups have already looked into the intratumoural distribution of Nbs. For example, both Bannas et al. and Oliveria et al. used *ex vivo* fluorescence microscopy (respectively confocal microscopy and flatbed near-infrared fluorescence scanning) to compare the penetration of fluorescently-labeled Nbs and mAbs targeting tumour antigen. They both found that within the first hours after injection, homogenous staining of the tumour cells could be achieved with the Nb, whereas the mAb was not capable of achieving a similar homogeneity, even after 24 h [28,29].

More recently, Hernandez et al. also demonstrated, using tumour spheroids grown *in vitro,* that a more rapid and homogenous distribution was achieved with the monomeric Nb as compared to the dimeric Nb and especially the mAb. This correlated with *in vivo* nuclear imaging and *ex vivo* autoradiography data obtained in tumour xenografts. While such spheroids are an elegant method to evaluate effects related to diffusion and affinity in a more standardized manner, they are still significantly different from the *in vivo* situation. Due to the absence of vasculature, extravasation as well as plasma and tumour clearance are not considered.

Results obtained using an *in vivo* dorsal window chamber model as in the present study may nevertheless differ in the degree of vascularization, permeability of the vasculature, or the amount of stromal tissue, depending on the tumour cell line chosen. The use of orthotopic or patient-derived xenografts may furthermore better mimic the heterogeneity of human tumours. Complex theoretical models, proposed to quantitatively evaluate tumour distribution [39], could unfortunately not be applied in this study since our data set did not permit the estimation of parameters and coefficients needed to account for processes such as blood clearance, extravasation, diffusion, specific binding, internalization, catabolism, or lymphatic clearance [7]. The difficulty stems from the limited axial resolution of the 2D intravital images, in

combination with the complex 3D structure of the vascular tree and possible deformation of the area-of-interest over time. However, ultimately, the goal of this study was not to estimate physically meaningful parameters but to qualitatively characterize and differentiate the distribution of the different tracers through the tumour.

Further studies should investigate the effect of using tumours with different vascular permeability, as well as Nbs with differing degrees of internalization, and different affinity constants (K_D-values), as well as association and dissociation rates (k_a and k_d) on the intratumoural distribution, as for structurally similar compounds, affinity characteristics can significantly influence tumour penetration. When previously two single chain variable fragments (scFv), one with an affinity of 30 pM and another with 8 nM affinity, were applied at the same concentration on tumour spheroids, the lower affinity scFv distributed much more homogenously than the high affinity scFv [40], indicating that even monovalent compounds can show a barrier-site effect when their affinity is too high.

Another interesting avenue of research, is in determining the tumour distribution of blood half-life extended Nbs. These have been proposed for use in therapeutic applications, as the slower systemic clearance should allow them to have an overall greater tumour uptake. Their greater size may, however prevent a homogenous intratumoural distribution, although in a study of Tijink et al., a trimeric Nb construct, containing a bivalent anti-EGFR Nb and a monovalent albumin-binding domain appeared to be able to penetrate more homogenously than cetuximab from 6 h post-injection, based on *ex vivo* Immunohistochemistry [41].

Our observations carry broad implications for the medical use of Nb tracers and their design to this end. For nuclear medicine imaging applications, molecular tracers that penetrate fast and deep into tumour tissue and for which the unbound tracer is rapidly cleared allow fast and reliable patient stratification and predictive imaging. Detected tumour heterogeneity could confidently be attributed to zones with heterogeneous biomarker expression or necrotic or hypoxic areas that are difficult to access and thus require more aggressive treatment. Generally, these advantages may extend to fluorescence molecular imaging applications as well, though there can be some debate on whether or not deep tumour penetration is absolutely essential for highlighting tumour margins during surgery.

For therapy, a homogenous intratumoural distribution as seen with the monomeric specific Nbs, implies that fewer tumour cells remain untreated and thus escape therapy [7,42]. This may be especially relevant to therapies with a short range of action, such as toxins or α-particle emitting radionuclides [43]. In case a prolonged local therapeutic effect is warranted, bivalent agents that are retained for longer in the tumour might be chosen. Their heterogenous tissue distribution could possibly be compensated by the bystander effect, the principle of a therapeutic effect being indirectly caused by factors released through stress or death of adjacent cells [44]. Additionally, β-emitting radioisotopes with longer path-lengths could here allow an extra therapeutic effect by crossfire radiation [45]. Repetitive injection of monovalent Nb-based drugs or efficiently internalizing monovalent Nbs with residualizing therapeutic moieties to compensate for their faster tumour wash-out, may be valid alternatives.

Finally, to specifically block easily accessible on-target off-tumour binding sites, a monovalent targeting Nb could be co-injected with an excess of its bivalent analogue. This strategy has previously been applied to reduce the high specific extratumoural uptake in liver or spleen of a macrophage mannose receptor-specific Nb, while tumour uptake remained unaffected [31]. In the spleen and liver, MMR is highly intra- and perivascularly expressed, and so can be conveniently blocked by a bivalent Nb. The monovalent Nb can then reach the MMR-expressing macrophages in the deeper lying hypoxic regions of the tumour faster than the bivalent. An analogous strategy was applied using anti-human epidermal growth factor receptor 3 (HER3) affibodies. When injected in low molar excess, a trivalent variant could reduce specific accumulation of a radiolabeled anti-HER3 affibody in the liver while retaining tumour targeting and enhancing the tumour-to-background ratio [46].

5. Conclusion

This study demonstrates for the first time longitudinally and *in vivo*, that Nbs, contrarily to intact Abs, are able to penetrate very rapidly and deeply into tumour tissue. These findings underline the potential of monomeric Nbs in targeted therapies and molecular imaging applications. Since an increase in size and valency can significantly impact the tumour penetration and distribution of Nbs, these factors should be taken into account during the design of novel tracers and therapeutics.

Supplementary data to this article can be found online at https://doi.org/10.1016/j.jconrel.2019.11.014.

Funding

This research is supported by the scientific fund Willy Gepts (WFWG), Stichting Tegen Kanker (STK), Vlaamse Liga tegen Kanker (VLK), and the Oncology Research Center (ORC, VUB). Tony Lahoutte is a senior clinical investigator and Matthias D'Huyvetter is a postdoctoral fellow of the Research Foundation – Flanders (FWO), Belgium. Patrice Mollard is supported by grants from France-Bioimaging (INBS10-GaL/AR-11/12), Institut National de la Santé et de la Recherche Médicale, Centre National de la Recherche Scientifique (CNRS), and Université de Montpellier. Fijs van Leeuwen has received a Vici-grant from the Nederlandse Organisatie voor Wetenschappelijk Onderzoek (NWO).

Declaration of Competing Interest

Matthias D'Huyvetter, Nick Devoogdt and Tony Lahoutte are employees or consultants of Camel-IDS and hold ownership interest (including patents) in VHH radiotherapeutics.

Acknowledgements

We thank Muriel Busson, Cindy Peleman and Jan De Jonge for their assistance with this project.

References

[1] L.M. Weiner, R. Surana, S. Wang, Monoclonal antibodies: versatile platforms for cancer immunotherapy, Nat. Rev. Immunol. 10 (2010) 317–327, https://doi.org/10.1038/nri2744.
[2] A.J. Gunn, M.W. Brechbiel, P.L. Choyke, The emerging role of molecular imaging and targeted therapeutics in peritoneal carcinomatosis, Expert. Opin. Drug Deliv. 4 (2007) 389–402, https://doi.org/10.1517/17425247.4.4.389.
[3] J.K. Tunggal, D.S.M. Cowan, H. Shaikh, I.F. Tannock, Penetration of anticancer drugs through solid tissue: a factor that limits the effectiveness of chemotherapy for solid tumors, Clin. Cancer Res. 5 (1999) 1583–1586.
[4] R.K. Jain, Vascular and interstitial barriers to delivery of therapeutic agents in tumors, Cancer Metastasis Rev. 9 (1990) 253–266, https://doi.org/10.1007/BF00046364.
[5] Y. Matsumura, H. Maeda, A new concept for macromolecular therapeutics in cancer chemotherapy: mechanism of tumoritropic accumulation of proteins and the antitumor agents Smancs, Cancer Res. 46 (1986) 6387–6392, https://doi.org/10.1021/bc100070g.
[6] R.K. Jain, Barriers to drug delivery in tumors, Sci. Am. 271 (1994) 58–65.
[7] G.M. Thurber, M.M. Schmidt, K.D. Wittrup, Factors determining antibody distribution in tumors, Trends Pharmacol. Sci. 29 (2008) 57–61, https://doi.org/10.1016/j.tips.2007.11.004.
[8] W. van Osdol, K. Fujimori, J.N. Weinstein, An analysis of monoclonal antibody distribution in microscopic tumor nodules: consequences of a "binding site barrier", Cancer Res. 51 (1991) 4776–4784.
[9] T. Saga, R.D. Neumann, T. Heya, et al., Targeting cancer micrometastases with monoclonal antibodies: a binding-site barrier, Proc. Natl. Acad. Sci. U. S. A. 92 (1995) 8999–9003, https://doi.org/10.1073/pnas.92.19.8999.
[10] J. Sato, W. van Osdol, J.N. Weinstein, M.J. Perez-Bacete, Micropharmacology of monoclonal antibodies in solid tumors: direct experimental evidence for a binding site barrier, Cancer Res. 52 (1992) 5144–5153.
[11] A.M. Wu, Engineered antibodies for molecular imaging of cancer, Methods 65 (2014) 139–147, https://doi.org/10.1016/j.ymeth.2013.09.015.
[12] K.T. Xenaki, S. Oliveira, P.M.P. van Bergen en Henegouwen, Antibody or antibody

fragments: implications for molecular imaging and targeted therapy of solid tumors, Front. Immunol. (2017), https://doi.org/10.3389/fimmu.2017.01287.
[13] A.C. Freise, A.M. Wu, In vivo imaging with antibodies and engineered fragments, Mol. Immunol. 67 (2015) 142–152, https://doi.org/10.1016/j.molimm.2015.04.001.
[14] Z. Li, B.F. Krippendorff, S. Sharma, et al., Influence of molecular size on tissue distribution of antibody fragments, MAbs 8 (2016) 113–119, https://doi.org/10.1080/19420862.2015.1111497.
[15] R. Muchekehu, D. Liu, M. Horn, et al., The effect of molecular weight, PK, and valency on tumor biodistribution and efficacy of antibody-based drugs, Transl. Oncol. 6 (2013) 562–IN6, https://doi.org/10.1593/tlo.13409.
[16] S.I. Rudnick, J. Lou, C.C. Shaller, et al., Influence of affinity and antigen internalization on the uptake and penetration of anti-HER2 antibodies in solid Tumors, Cancer Res. 71 (2011) 2250–2259, https://doi.org/10.1158/0008-5472.CAN-10-2277.
[17] S. Muyldermans, T.N. Baral, V.C. Retamozzo, et al., Camelid immunoglobulins and nanobody technology, Vet. Immunol. Immunopathol. 128 (2009) 178–183, https://doi.org/10.1016/j.vetimm.2008.10.299.
[18] C. Hamers-Casterman, T. Atarhouch, S. Muyldermans, et al., Naturally occurring antibodies devoid of light chains, Nature 363 (1993) 446–448, https://doi.org/10.1038/363446a0.
[19] P. Debie, N. Devoogdt, S. Hernot, Targeted nanobody-based molecular tracers for nuclear imaging and image-guided surgery, Antibodies 8 (2019) 12, https://doi.org/10.3390/antib8010012.
[20] J. De Vos, N. Devoogdt, T. Lahoutte, S. Muyldermans, Camelid single-domain antibody-fragment engineering for (pre)clinical *in vivo* molecular imaging applications: adjusting the bullet to its target, Expert. Opin. Biol. Ther. 13 (2013) 1149–1160, https://doi.org/10.1517/14712598.2013.800478.
[21] A. Krasniqi, M. D'Huyvetter, C. Xavier, et al., Theranostic radiolabeled anti-CD20 sdAb for targeted radionuclide therapy of non-Hodgkin lymphoma, Mol. Cancer Ther. 16 (2017) 2828–2839, https://doi.org/10.1158/1535-7163.MCT-17-0554.
[22] M.M. Kijanka, A.S.A. van Brussel, E. van der Wall, et al., Optical imaging of pre-invasive breast cancer with a combination of VHHs targeting CAIX and HER2 increases contrast and facilitates tumour characterization, EJNMMI Res. (2016), https://doi.org/10.1186/s13550-016-0166-y.
[23] M. Kijanka, F.J. Warnders, M. El Khattabi, et al., Rapid optical imaging of human breast tumour xenografts using anti-HER2 VHHs site-directly conjugated to IRDye 800CW for image-guided surgery, Eur. J. Nucl. Med. Mol. Imaging 40 (2013) 1718–1729, https://doi.org/10.1007/s00259-013-2471-2.
[24] M. D'Huyvetter, J. De Vos, C. Xavier, et al., 131I-labeled anti-HER2 camelid sdAb as a theranostic tool in cancer treatment, Clin. Cancer Res. 23 (2017) 6616–6628, https://doi.org/10.1158/1078-0432.CCR-17-0310.
[25] P. Debie, J. Van Quathem, I. Hansen, et al., Effect of dye and conjugation chemistry on the biodistribution profile of near-infrared-labeled nanobodies as tracers for image-guided surgery, Mol. Pharm. 14 (2017) 1145–1153, https://doi.org/10.1021/acs.molpharmaceut.6b01053.
[26] C. Xavier, A. Blykers, D. Laoui, et al., Clinical translation of [68Ga]Ga-NOTA-anti-MMR-sdAb for PET/CT imaging of protumorigenic macrophages, Mol. Imaging Biol. (2019) 898–906, https://doi.org/10.1007/s11307-018-01302-5.
[27] P. Debie, M. Vanhoeij, N. Poortmans, et al., Improved debulking of peritoneal tumor implants by near-infrared fluorescent nanobody image guidance in an experimental mouse model, Mol. Imaging Biol. 20 (2018) 361–367, https://doi.org/10.1007/s11307-017-1134-2.
[28] P. Bannas, A. Lenz, V. Kunick, et al., Molecular imaging of tumors with nanobodies and antibodies: timing and dosage are crucial factors for improved in vivo detection, Contrast Media Mol. Imag. 10 (2015) 367–378, https://doi.org/10.1002/cmmi.1637.
[29] S. Oliveira, G.A.M.S. Van Dongen, M. Stigter-Van Walsum, et al., Rapid visualization of human tumor xenografts through optical imaging with a near-infrared fluorescent anti-epidermal growth factor receptor nanobody, Mol. Imaging 11 (2012) 33–46, https://doi.org/10.2310/7290.2011.00025.
[30] A. Krasniqi, M. Bialkowska, C. Xavier, et al., Pharmacokinetics of radiolabeled dimeric sdAbs constructs targeting human CD20, New Biotechnol. 45 (2018) 69–79, https://doi.org/10.1016/j.nbt.2018.03.004.
[31] K. Movahedi, S. Schoonooghe, D. Laoui, et al., Nanobody-based targeting of the macrophage mannose receptor for effective in vivo imaging of tumor-associated macrophages, Cancer Res. 72 (2012) 4165–4177, https://doi.org/10.1158/0008-5472.CAN-11-2994.
[32] I.B. Hernández, R. Rompen, R. Rossin, et al., Imaging of Tumor Spheroids, Dual-Isotope SPECT, and Autoradiographic Analysis to Assess the Tumor Uptake and Distribution of Different Nanobodies, (2019), https://doi.org/10.1007/s11307-019-01320-x.
[33] I. Vaneycken, N. Devoogdt, N. Van Gassen, et al., Preclinical screening of anti-HER2 nanobodies for molecular imaging of breast cancer, FASEB J. 25 (2011) 2433–2446, https://doi.org/10.1096/fj.10-180331.
[34] M. Lemaire, M. D'Huyvetter, T. Lahoutte, et al., Imaging and radioimmunotherapy of multiple myeloma with anti-idiotypic nanobodies, Leukemia 28 (2014) 444–447, https://doi.org/10.1038/leu.2013.292.
[35] A. Bunschoten, D.M. Van Willigen, T. Buckle, et al., Tailoring fluorescent dyes to optimize a hybrid RGD-tracer, Bioconjug. Chem. 27 (2016) 1253–1258, https://doi.org/10.1021/acs.bioconjchem.6b00093.
[36] S.J. Spa, A.W. Hensbergen, S. van der Wal, et al., Computational and experimental data on electrostatic density and stacking tendency of asymmetric cyanine 5 dyes, Data Br. 22 (2019) 50–55, https://doi.org/10.1016/j.dib.2018.11.132.
[37] S.J. Spa, A.W. Hensbergen, S. van der Wal, et al., The influence of systematic structure alterations on the photophysical properties and conjugation characteristics of asymmetric cyanine 5 dyes, Dyes Pigments 152 (2018) 19–28, https://doi.org/10.1016/j.dyepig.2018.01.029.
[38] A. Ibrahimi, G. Vande Velde, V. Reumers, et al., Highly efficient multicistronic lentiviral vectors with peptide 2A sequences, Hum. Gene Ther. 860 (2009) 845–860.
[39] G.M. Thurber, S.C. Zajic, K.D. Wittrup, Theoretic criteria for antibody penetration into solid tumors and micrometastases, J. Nucl. Med. 48 (2007) 995–999, https://doi.org/10.2967/jnumed.106.037069.
[40] G.M. Thurber, K.D. Wittrup, Quantitative spatiotemporal analysis of antibody fragment diffusion and endocytic consumption in tumor spheroids, Cancer Res. 68 (2008) 3334–3341, https://doi.org/10.1158/0008-5472.CAN-07-3018.Quantitative.
[41] B.M. Tijink, T. Laeremans, M. Budde, et al., Improved tumor targeting of anti-epidermal growth factor receptor Nanobodies through albumin binding: taking advantage of modular Nanobody technology, Mol. Cancer Ther. 7 (2008) 2288–2297, https://doi.org/10.1158/1535-7163.MCT-07-2384.
[42] C. Cilliers, B. Menezes, I. Nessler, et al., Improved Tumor Penetration and Single-Cell Targeting of Antibody – Drug Conjugates Increases Anticancer Ef fi cacy and Host Survival, 78 (2018), pp. 758–769, https://doi.org/10.1158/0008-5472.CAN-17-1638.
[43] Y. Dekempeneer, M. Keyaerts, A. Krasniqi, et al., Targeted alpha therapy using short-lived alpha-particles and the promise of nanobodies as targeting vehicle, Expert. Opin. Biol. Ther. 16 (2016) 1035–1047, https://doi.org/10.1080/14712598.2016.1185412.
[44] M. Boyd, A. Sorensen, A.G. McCluskey, R.J. Mairs, Radiation quality-dependent bystander effects elicited by targeted radionuclides, J. Pharm. Pharmacol. 60 (2008) 951–958, https://doi.org/10.1211/jpp.60.8.0002.
[45] I. Navarro-Teulon, C. Lozza, A. Pèlegrin, et al., General overview of radioimmunotherapy of solid tumors, Immunotherapy 5 (2013) 467–487, https://doi.org/10.2217/imt.13.34.
[46] M. Rosestedt, K.G. Andersson, S.S. Rinne, et al., Improved contrast of affibody-mediated imaging of HER3 expression in mouse xenograft model through co-injection of a trivalent affibody for in vivo blocking of hepatic uptake, Sci. Rep. 9 (2019) 1–10, https://doi.org/10.1038/s41598-019-43145-2.